PHYSICAL REVIEW B **95**, 134405 (2017)

Spin dynamics in the antiferromagnetic phases of the Dirac metals $A\mathrm{MnBi}_2$ (A = Sr, Ca)

M. C. Rahn,[1,*] A. J. Princep,[1] A. Piovano,[2] J. Kulda,[2] Y. F. Guo,[3,4] Y. G. Shi,[5] and A. T. Boothroyd[1,†]
[1]*Clarendon Laboratory, Department of Physics, University of Oxford, Oxford OX1 3PU, England, United Kingdom*
[2]*Institut Laue-Langevin, 6 rue Jules Horowitz, 38042 Grenoble Cedex 9, France*
[3]*School of Physical Science and Technology, ShanghaiTech University, Shanghai 201210, China*
[4]*CAS Center for Excellence in Superconducting Electronics (CENSE), Shanghai 200050, China*
[5]*Beijing National Laboratory for Condensed Matter Physics, Institute of Physics, Chinese Academy of Sciences, Beijing 100190, China*

(Received 24 November 2016; revised manuscript received 6 March 2017; published 4 April 2017)

The square Bi layers in $A\mathrm{MnBi}_2$ (A = Sr, Ca) host Dirac fermions which coexist with antiferromagnetic order on the Mn sublattice below $T_\mathrm{N} = 290$ K (Sr) and 265 K (Ca). We have measured the spin-wave dispersion in these materials by triple-axis neutron spectroscopy. The spectra show pronounced spin gaps of 10.2(2) meV (Sr) and 8.3(8) meV (Ca) and extend to a maximum energy transfer of 61–63 meV. The observed spectra can be accurately reproduced by linear spin-wave theory from a Heisenberg effective spin Hamiltonian. Detailed global fits of the full magnon dispersion are used to determine the in-plane and interlayer exchange parameters as well as well as the magnetocrystalline anisotropy constant. To within experimental error we find no evidence that the magnetic dynamics are influenced by the Dirac fermions.

DOI: 10.1103/PhysRevB.95.134405

I. INTRODUCTION

Following the observation of the topological properties of electrons on the honeycomb layers of graphene, the universal characteristics of massless dispersing low-energy quasiparticles have been realized across a variety of condensed-matter systems. The ternary bismuthides $A\mathrm{MnBi}_2$ (A = Ca, Sr) [1–4] are a recent addition to this family of so-called Dirac materials. The Bi square layers of $A\mathrm{MnBi}_2$ have been found to show the same unusual transport characteristics as graphene or topological insulators [5–8]. Due to the suppression of backscattering processes, the electronic and thermal conductivities are enhanced, and the large separation of Landau levels produces a large linear magnetoresistance. Indeed, angle-resolved photoemission spectroscopy (ARPES) has provided direct evidence of the linear band crossings in both SrMnBi_2 and CaMnBi_2 [9,10], with a highly anisotropic Dirac cone.

Among other Dirac materials, these bismuthides attract special interest because their Dirac fermions may couple to magnetically active transition-metal states, promising an indirect experimental handle to tune the topological bands. Below $T_\mathrm{N}^\mathrm{Sr} \simeq 290$ K and $T_\mathrm{N}^\mathrm{Ca} \simeq 265$ K, the large divalent Mn ($3d^5$, $S = 5/2$) magnetic moments of magnitude $\approx 3.7\,\mu_\mathrm{B}$ in these materials align parallel to the c axis and form antiferromagnetic structures [11]. The two compounds were found to differ in the sign of their interlayer coupling, resulting in ferro- and antiferromagnetic stacking of Néel-ordered layers in CaMnBi_2 and SrMnBi_2, respectively [11]. An interpretation based on first-principles calculations suggests that in the ferromagnetically stacked case (CaMnBi_2), the Dirac bands may provide an itinerant interlayer exchange path and thus directly couple to the magnetic ground state [11]. This appeared to be supported by a weak resistivity anomaly observed at T_N in CaMnBi_2, but not in SrMnBi_2 [11]. Earlier transport studies, however, had not registered such an anomaly in either SrMnBi_2 [4] or CaMnBi_2 [12,13].

In metallic magnets a coupling between the ordered magnetic moments and conduction electron states can reveal itself in the magnetic excitation spectrum. For example, there can be damping due to spin-wave decay into the Stoner continuum, anomalies in the magnon dispersion due to modifications of the exchange interactions by conduction electron states, or gap formation due to an additional Kondo energy scale.

Here we report on a single-crystal neutron inelastic scattering study of SrMnBi_2 and CaMnBi_2 in the magnetically ordered state. Our analysis shows that the magnon spectrum in both materials can be accurately reproduced from a Heisenberg model describing a local-moment, quasi-two-dimensional (2D) antiferromagnet. The model includes nearest- and next-nearest-neighbor in-plane exchange interactions and a weak interlayer exchange interaction, together with an easy-axis anisotropy. We did not find any anomalies that would suggest significant coupling between the magnons and conduction electron states. The interlayer coupling is smaller than found in the reference compound $\mathrm{BaMn}_2\mathrm{Bi}_2$, consistent with the larger separation of the Mn spins along the c axis in $A\mathrm{MnBi}_2$.

II. EXPERIMENTAL DETAILS

The preparation and characterization of the single crystals used in the experiments has been reported previously [11]. Polycrystalline $A\mathrm{MnBi}_2$ was first synthesized by solid-state reaction of the elements. Single crystals were then grown from self-flux in an alumina crucible. Electron-probe microanalysis confirmed near-ideal stoichiometry, with a small ($\approx$2%) Bi deficiency in the Sr compound (for details, see Ref. [11]). Laboratory x-ray-diffraction measurements confirmed the tetragonal crystal structures reported previously [1,2], space groups $I4/mmm$ (SrMnBi_2) and $P4/nmm$ (CaMnBi_2) (see Fig. 1). Magnetization measurements on the batch of crystals used here were consistent with previous studies (see Ref. [14]).

Neutron inelastic measurements were performed at the Institut Laue-Langevin on the triple-axis neutron spectrometer

---

[*] marein.rahn@physics.ox.ac.uk

[†] a.boothroyd@physics.ox.ac.uk

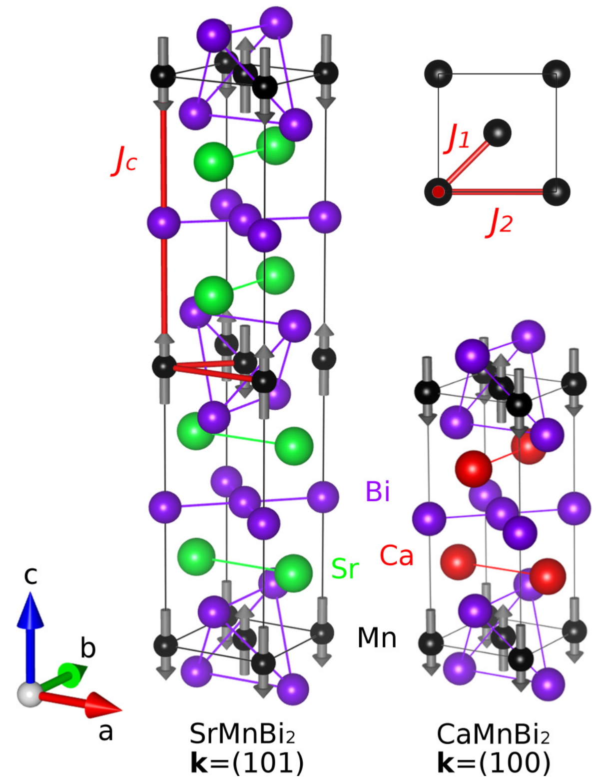

FIG. 1. The crystal and magnetic structures of $\mathrm{SrMnBi_2}$ ($a \approx 4.58\,\mathrm{\AA}$, $c \approx 23.14\,\mathrm{\AA}$, magnetic space group $I4'/m'm'm$) and $\mathrm{CaMnBi_2}$ ($a \approx 4.50\,\mathrm{\AA}$, $c \approx 11.07\,\mathrm{\AA}$, magnetic space group $P4'/n'm'm$) [11]. The magnetic propagation vectors $\mathbf{k}$ indicated in this figure describe the magnetic structures $\mathbf{m}(\mathbf{r}_j)$ (in lattice coordinates $\mathbf{r}_j$) by the relation $\mathbf{m}(\mathbf{r}_j) = \mathbf{m}(0)\,\exp(2\pi\mathrm{i}\,\mathbf{k}\cdot\mathbf{r}_j)$, where $\mathbf{m}(0)$ is the magnetic moment at an arbitrary origin located on a Mn site. For clarity, the origin of the $\mathrm{SrMnBi_2}$ unit cell has been shifted by $(\frac{1}{2},0,\frac{1}{4})$ relative to the conventional cell. The exchange paths J_1, J_2, and J_c are indicated by red lines.

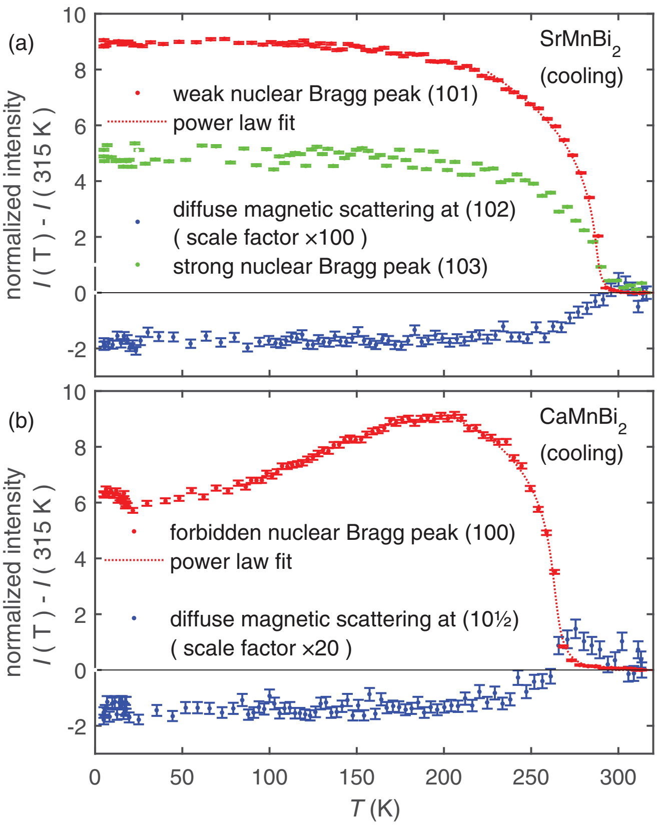

FIG. 2. Temperature dependence of the difference intensity $I(T) - I(315\,\mathrm{K})$ at selected wave vectors (see legend), recorded while cooling (a) $\mathrm{SrMnBi_2}$ and (b) $\mathrm{CaMnBi_2}$. Power-law fits to the Bragg peaks yield transition temperatures of $T_\mathrm{N}^\mathrm{Sr} = 287(5)\,\mathrm{K}$ and $T_\mathrm{N}^\mathrm{Ca} = 264(2)\,\mathrm{K}$. Above T_N, incipient in-plane correlations contribute diffuse rods of magnetic scattering along $(10L)$. These fluctuations are enhanced towards T_N (critical scattering) and then freeze out with the onset of interplane order (blue symbols). The decrease in intensity of the (100) reflection of $\mathrm{CaMnBi_2}$ below 200 K is not consistent with previous data and should be disregarded (see main text).

IN8 [15] with the FlatCone detector [16]. By keeping the outgoing energy fixed and recording rocking scans at various incident energies, this setup allows an efficient collection of constant energy-transfer maps covering a wide range of reciprocal space. The FlatCone array of analyzer crystals and helium tube detectors consists of 31 channels spaced by 2.5°, thus covering a 75° range of scattering angle. Throughout the study, the FlatCone was used with its Si (111) analyzer crystals selecting a fixed outgoing wave vector of $k_\mathrm{f} = 3\,\mathrm{\AA}^{-1}$ ($E_\mathrm{f} = 18.6\,\mathrm{meV}$). For energy transfers below and above 40 meV (incoming energies $E_\mathrm{i} \gtrless 58.6\,\mathrm{meV}$), the double-focusing Si (111) and pyrolitic graphite (002) monochromators were used, respectively. In four separate experiments, the scattering from the $\mathrm{SrMnBi_2}$ and $\mathrm{CaMnBi_2}$ single crystals (of mass 3.3 and 1.6 g, respectively) was investigated in the $(HK0)$ (ab orientation) and $(H0L)$ (ac orientation) scattering planes. Throughout this paper we give wave vectors in reciprocal lattice units (r.l.u.) $\mathbf{q} = (H,K,L) \equiv (H \times 2\pi/a, K \times 2\pi/b, L \times 2\pi/c)$. The samples were mounted in a standard top-loading liquid helium cryostat. All spectra were recorded at a sample temperature of approximately 5 K.

III. RESULTS AND ANALYSIS

While cooling the samples in the ac orientation, we tracked the intensities at selected positions in the $(H0L)$ plane of reciprocal space. Figures 2(a) and 2(b) show the resulting temperature dependences for $\mathrm{SrMnBi_2}$ and $\mathrm{CaMnBi_2}$, respectively. This includes the magnetic Bragg contribution at (101) and (103) (for Sr) and (100) (for Ca), as well as the diffuse magnetic scattering at another position along the $(10L)$ direction away from the Bragg condition. The data, here represented as the relative change in the intensity, demonstrate the order-parameter characteristics of magnetic Bragg scattering at the antiferromagnetic transitions. We note that the decrease of the $\mathrm{CaMnBi_2}$ (100) magnetic scattering below 200 K is not consistent with our previous powder neutron-diffraction data [11], which could be due to a shift of the peak between two detector channels as the lattice contracts.

Above the ordering temperature, incipient in-plane magnetic correlations form diffuse rods of magnetic scattering along the c^* direction of reciprocal space, as revealed at the $(10L)$ non-Bragg positions. When cooling towards T_N, this

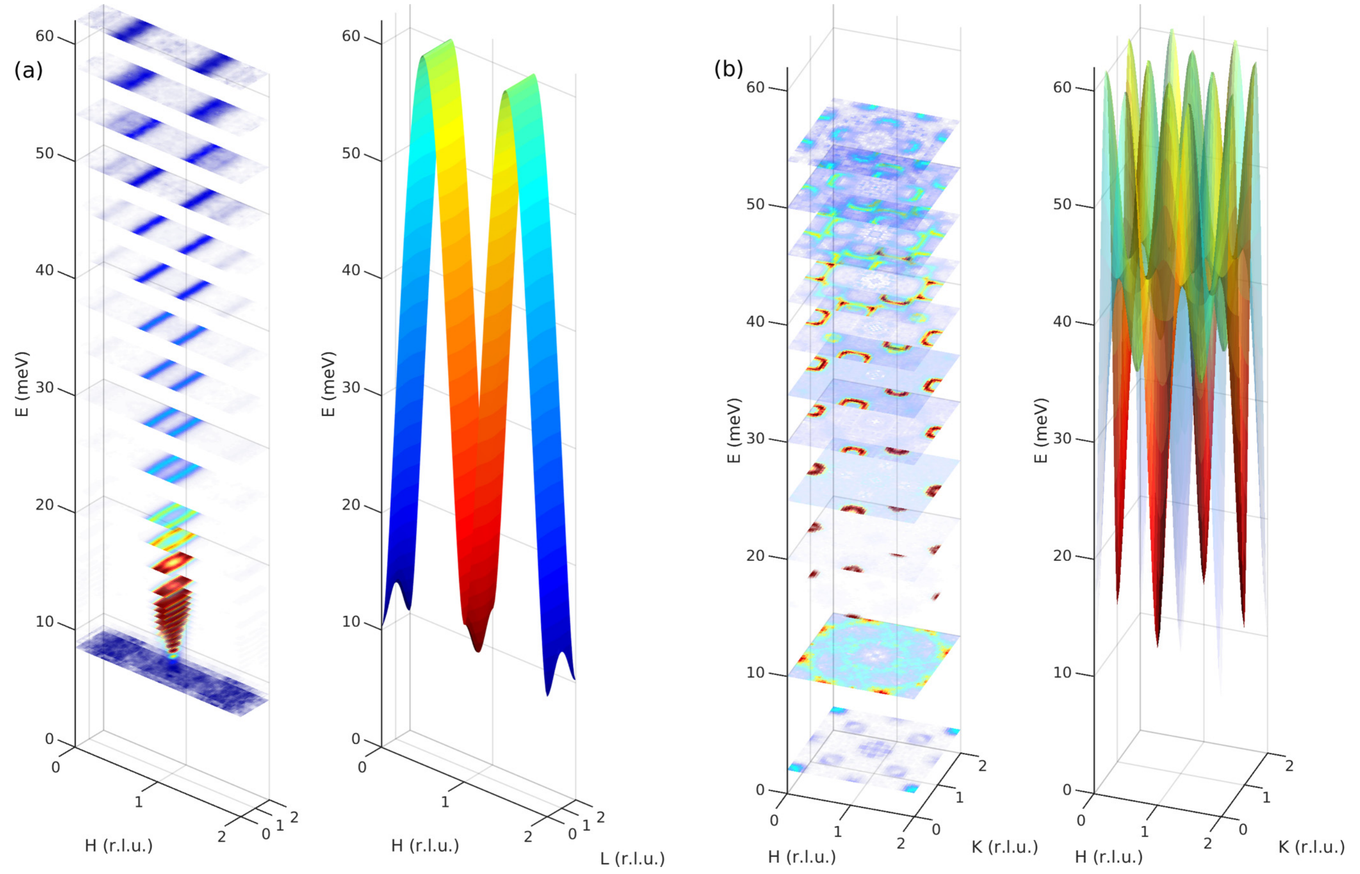

FIG. 3. Magnon spectrum of $SrMnBi_2$ in the (a) $(H0L)$ and (b) $(HK0)$ planes in reciprocal space. The data are illustrated by a stacking plot of constant-energy slices (left panels), and the best-fit spin-wave model is represented by the corresponding dispersion surface (right panels). A more quantitative comparison between data and simulation is provided in Ref. [14].

diffuse scattering initially intensifies and then subsides when the weaker interlayer correlations set in and neutron spectral weight is confined to the Bragg peaks. Fitting a power law to the thermal variation of the (101) (Sr) and (100) (Ca) peaks yields Néel temperatures of $T_N^{Sr} = 287(5)$ K and $T_N^{Ca} = 264(2)$ K. These values are consistent with previous single-crystal bulk measurements of transport and ARPES samples [4,9,12,13], but differ slightly from the values found in our earlier neutron powder diffraction study [11]. This difference is likely due to small structural or compositional variations among the samples. The critical exponents $\beta^{Sr} = 0.15(3)$ and $\beta^{Ca} = 0.11(2)$ obtained from the power-law fit are much smaller than the value $\beta = 0.365$ of the three-dimensional Heisenberg model, indicating the reduced dimensionality of the magnetism in these systems. Due to the additional bismuth layers in the unit cells, the magnetism is more two dimensional in $A\mathrm{MnBi}_2$ than in the related (122) manganese arsenide $BaMn_2As_2$, $\beta = 0.35(2)$ [17]. Instead, the interlayer correlations compare well to the parent compounds of (122) iron-based superconductors, e.g., $\beta = 0.098(1)$ for $SrFe_2As_2$ [18] and $\beta = 0.125$ for $BaFe_2As_2$ [19]. A detailed description of the power-law fit to this data is provided in Ref. [14].

The measured neutron spectra are summarized in Figs. 3 ($SrMnBi_2$) and 4 ($CaMnBi_2$). A more quantitative presentation of the data is provided in Figs. S2–S5 of Ref. [14]. Due to the periodicity of the antiferromagnetic order, the magnetic zone centers are located at (HKL) positions with $(H+K)$ and L both odd integers for $SrMnBi_2$, and at positions with $(H+K)$ odd and L any integer for $CaMnBi_2$. For both compounds, the spectra reveal a well-defined magnon dispersion above spin gaps of approximately 10 meV (Sr) and 8 meV (Ca). The magnons are highly dispersive parallel to the layers, but only weakly dispersive perpendicular to the layers. For both samples the magnon bandwidth is around 50 meV for spin waves propagating in the $(HK0)$ plane and 3–4 meV along $(10L)$. Figure 5 represents more quantitatively the magnon dispersion in the $(HK0)$ plane as obtained from Gaussian fits to constant-energy cuts, and the left-hand panels of Figs. 6(a) and 6(b) illustrate the out-of-plane dispersion by energy-wave-vector slices of the data along the $(10L)$ direction.

To obtain quantitative information on the magnetic couplings we have compared the data with the linear spin-wave spectrum calculated from an effective spin Hamiltonian that includes a Heisenberg coupling term and an Ising-like single-ion anisotropy:

$$\hat{\mathcal{H}} = \sum_{\langle i,j\rangle} J_{ij}\hat{\mathbf{S}}_i \cdot \hat{\mathbf{S}}_j - \sum_i D\left(\hat{S}_i^z\right)^2, \qquad (1)$$

where we include nearest-neighbor (J_1) and next-nearest-neighbor (J_2) exchange constants, an interlayer exchange interaction J_c, and the anisotropy constant D. The exchange paths are shown in Fig. 1. Using the Holstein-Primakoff transformation of two interacting Bose fields, corresponding to the two collinear antiferromagnetic sublattices, we obtain

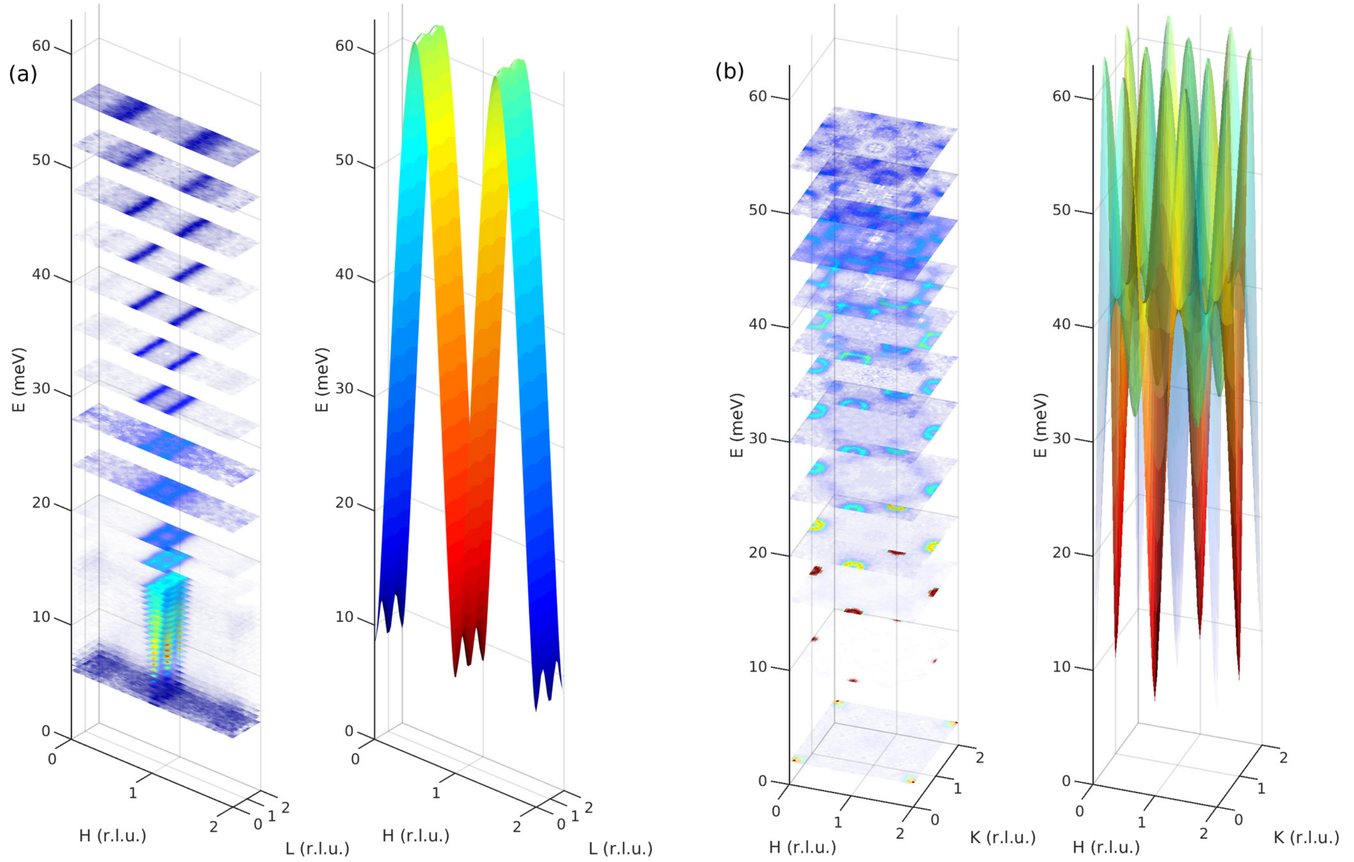

FIG. 4. Magnon spectrum of CaMnBi$_2$ presented in the same way as in Fig. 3.

the dispersion relation

$$E(\mathbf{q}) = \sqrt{A(\mathbf{q})^2 - B(\mathbf{q})^2} \tag{2}$$

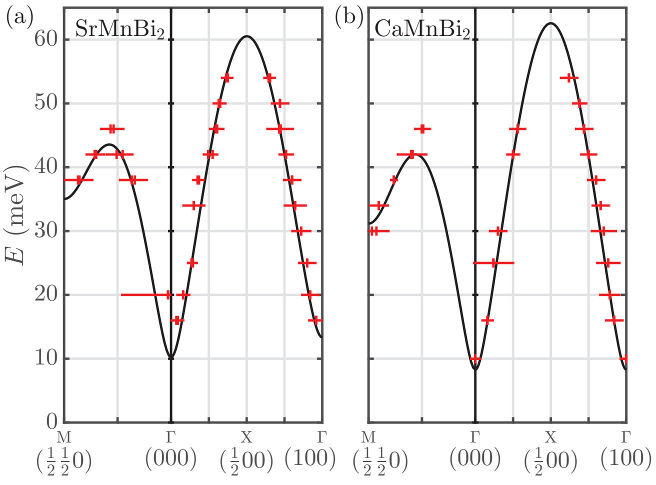

FIG. 5. Magnon dispersion along high-symmetry directions in the $(HK0)$ plane, for (a) SrMnBi$_2$ and (b) CaMnBi$_2$. The black line indicates the best fit from the linear spin-wave model. Red markers represent the position (vertical bars) and full width at half maximum (horizontal lines) of Gaussian fits to cuts through the raw data along the corresponding directions.

where $\mathbf{q}$ is the magnon wave vector,

$$A(\mathbf{q}) = S\,[\,\mathcal{J}_{\rm AF}(0) - \mathcal{J}_{\rm F}(0) + \mathcal{J}_{\rm F}(\mathbf{q}) + 2\,D\,],$$
$$B(\mathbf{q}) = S\ \mathcal{J}_{\rm AF}(\mathbf{q})$$

and

$$\mathcal{J}(\mathbf{q}) = \sum_n J_n\, \mathrm{e}^{2\pi\mathrm{i}\,\mathbf{q}\cdot\mathbf{r}_n} \tag{3}$$

is the Fourier transform of the exchange interactions. The subscripts F and AF refer to summation over ferromagnetically and antiferromagnetically aligned pairs of spins, respectively. The resulting differential scattering cross section for single-magnon creation is

$$\frac{d\sigma}{d\Omega d\omega} = \frac{k_{\rm f}}{k_{\rm i}}\left(\frac{\gamma r_0}{2}\right)^2 S(\mathbf{q},\omega), \tag{4}$$

$$S(\mathbf{q},\omega) = g^2 N S\,\frac{A(\mathbf{q}) - B(\mathbf{q})}{E(\mathbf{q})}\,\{n(\omega) + 1\}\,\delta\{\hbar\omega - E(\mathbf{q})\} \tag{5}$$

where $\hbar\omega$ is the neutron energy transfer, $k_{\rm f}$ and $k_{\mathbf{i}}$ are the outgoing and incoming neutron wave vectors, $\gamma = 1.913$, r_0 is the classical electron radius, g is the spectroscopic splitting factor, N is the number of magnetic ions per sublattice, S is the spin quantum number, and $n(\omega) = (\mathrm{e}^{\hbar\omega/k_{\rm B}T} - 1)^{-1}$ is the boson occupation number. Given the magnetic structures and exchange paths defined in Fig. 1, the explicit Fourier exchange

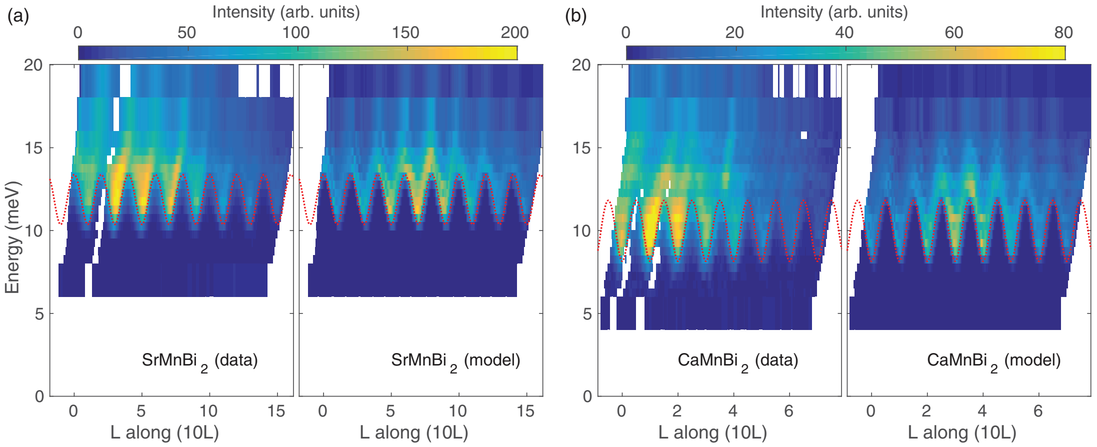

FIG. 6. Out-of-plane dispersion of the magnon spectra of (a) $SrMnBi_2$ and (b) $CaMnBi_2$, illustrated by slices along the $(10L)$ direction in reciprocal space (intensity averaged over the range $H = 0.95$–1.05 r.l.u.). The left-hand panels show interpolated plots of the data, and the right-hand panels give the corresponding best-fit spin-wave spectra convoluted with the instrumental resolution (for details, see text and Ref. [14]). The superimposed red dashed line indicates the theoretical dispersion using best-fit parameters.

terms for the case of $SrMnBi_2$ are

$$\mathcal{J}_{\rm AF}^{\rm Sr}(\mathbf{q}) = 2\,J_1\,[\cos(\pi\,H + \pi\,K) + \cos(\pi\,H - \pi\,K)] + 2\,J_c\,\cos(\pi\,L),$$

$$\mathcal{J}_{\rm F}^{\rm Sr}(\mathbf{q}) = 2\,J_2\,[\cos(2\pi\,H) + \cos(2\pi\,K)]$$

and, in the case of $CaMnBi_2$,

$$\mathcal{J}_{\rm AF}^{\rm Ca}(\mathbf{q}) = 2\,J_1\,[\cos(\pi\,H + \pi\,K) + \cos(\pi\,H - \pi\,K)],$$

$$\mathcal{J}_{\rm F}^{\rm Ca}(\mathbf{q}) = 2\,J_2\,[\cos(2\pi\,H) + \cos(2\pi\,K)] + 2\,J_c\,\cos(2\pi\,L).$$

This allows an analytical description of the spin gaps:

$$\Delta^{\rm Sr} \approx \Delta^{\rm Ca} \approx 4\sqrt{SJ_1}\sqrt{SD}, \tag{6}$$

where we have applied the appropriate approximations for the present case ($J_1 \gg J_c$, $J_1 \gg D$; for full expressions see Ref. [14]). Similarly, the bandwidth W of the dispersion along $(10L)$ is given by

$$W^{\rm Sr} \approx W^{\rm Ca} \approx 4\sqrt{SJ_1}\,(\sqrt{SD + 2\,|SJ_c|} - \sqrt{SD}). \tag{7}$$

If J_1 is the dominant exchange, as is found to be the case here, then the maximum of the in-plane dispersion is $\sim 4SJ_1$. Given J_1, we see from Eqs. (6) and (7) that in the relevant parameter regime the parameters D and J_c are determined by the size of the gap $\Delta^{\rm Sr/Ca}$ and bandwidth of the out-of-plane modulation $W^{\rm Sr/Ca}$, respectively. On the other hand, the balance between the parameters J_1 and J_2 determines details of the dispersion at higher energies in the $(HK0)$ plane. For example, a local minimum of the dispersion at the M point, $(\frac{1}{2},\frac{1}{2},0)$, as observed in both materials, will only occur for positive J_2, indicating a competition (frustration) between nearest- and next-nearest-neighbor exchange.

We find that the above model is able to reproduce very well all features in the data. For quantitative analysis we folded and averaged the raw constant-energy maps of reciprocal space into tiles of 2×2 r.l.u. With the data in this reduced form we could compare it to the model after convolution of the theoretical spectrum, Eqs. (4) and (5), with an energy- and wave-vector-dependent broadening function to take into account the instrumental resolution. A phenomenological Gaussian broadening of the analytical dispersion proved insufficient to achieve a consistent global fit to the data, particularly for the low-energy part of the magnetic dispersion in the *ac* plane. Instead, it was necessary to take into account the resolution of the triple-axis spectrometer, which was calculated with the RESTRAX ray-tracing algorithm [20,21].

Our procedure to determine the parameters of the spin Hamiltonian J_1, J_2, J_c, and D was carried out in three steps. First, a global fit of all data, using phenomenological Gaussian broadening of the dispersion, produced rough estimates of all parameters. Using these as starting values and fixing the in-plane exchange interactions J_1 and J_2, we obtained precise bounds on the interlayer exchange J_c and anisotropy D by fitting the resolution-convoluted spectrum for low energies (0–20 meV) to an energy–wave-vector slice with wave vector along $(10L)$, as illustrated in Fig. 6. Finally, J_1 and J_2 were refined by fitting the in-plane (*ab*) dispersion at high energies (30–44 meV) using Gaussian broadening.

Figure 5 provides a quantitative plot of the fits of the dispersions in the *ab* plane. A more detailed description of the data processing, fitting, and error estimation, and an explicit comparison of the data and best fits, are provided in Ref. [14].

IV. DISCUSSION

The exchange parameters for $SrMnBi_2$ and $CaMnBi_2$ obtained from the fits are summarized in Table I. Apart from the opposite sign of the interlayer exchange J_c, there are no significant differences between the parameters of $SrMnBi_2$ and $CaMnBi_2$. The absolute values of J_1 and J_2 are slightly larger in the case of $CaMnBi_2$, consistent with the smaller nearest-neighbor spacing ($d_{\rm NN}$). The magnitudes of J_c for the two compounds, which are the same to within the error, are much smaller than J_1 and J_2, confirming the quasi-2D character of the magnetism in these materials. Notably, these results are in good agreement with previous estimations based on first-principles calculations of the electronic structure,

TABLE I. Exchange parameters, magnetocrystalline anisotropy constants, and spin gaps of $\mathrm{SrMnBi_2}$ and $\mathrm{CaMnBi_2}$ obtained from a fit of the linear spin-wave model, as described in the text. The parameters can be related to the nearest-neighbor (d_{NN}) and interlayer (d_c) Mn-Mn atomic spacings, the ordered magnetic moment μ, and the ordering temperature T_{N} [11]. The corresponding values for two related Mn pnictides are reproduced below [22,23].

	SJ_1 (meV)	SJ_2 (meV)	SJ_c (meV)	SD (meV)	Δ (meV)	d_{NN} (Å)	d_c (Å)	$\mu(\mu_{\mathrm{B}})$	T_{N} (K)
$\mathrm{SrMnBi_2}$	21.3(2)	6.39(15)	0.11(2)	0.31(2)	10.2(2)	3.24	11.57	3.75(5)	287(5)
$\mathrm{CaMnBi_2}$	23.4(6)	7.9(5)	− 0.10(5)	0.18(3)	8.3(8)	3.18	11.07	3.73(5)	264(2)
$\mathrm{BaMn_2Bi_2}$ [22]	21.7(1.5)	7.85(1.4)	1.26(2)	0.87(15)[a]	16.29(26)	3.18	7.34	3.83(4)	387.2(4)
$\mathrm{BaMn_2As_2}$ [23]	33(3)	9.5(1.3)	3.0(6)			2.95	6.73	3.88(4)	625(1)

[a]The value of SD for $\mathrm{BaMn_2Bi_2}$ was misquoted in Ref. [22]. In this table we give the correct value [24].

which gave an average in-plane exchange of $SJ_{ab} \approx 30$ meV and $|SJ_c| \approx 0.3$ meV [11].

Regarding the magnetocrystalline anisotropy, we observe that D is enhanced by a factor 1.8 in $\mathrm{SrMnBi_2}$ compared with $\mathrm{CaMnBi_2}$. According to the initial structure determinations at room temperature [1,2], the local environment of the Mn ion is similar in both compounds: The $\mathrm{MnBi_4}$ tetrahedra are elongated by ≈14% along c and the ligand distances are $d^{\mathrm{Ca}}_{\mathrm{Mn-Bi}} = 2.87(1)$ Å and $d^{\mathrm{Sr}}_{\mathrm{Mn-Bi}} = 2.89(1)$ Å. The significant difference in anisotropy may therefore point to unknown structural distortions at 5 K (at present, no full refinement of crystallographic parameters at low temperatures is available). The anisotropy is in good agreement with the result of our earlier density functional prediction ($SD^{\mathrm{Ca}}_{\mathrm{DFT}} = 0.3$ meV [11]), as was also the case with the exchange constants.

It is instructive to compare the present results to two available inelastic neutron scattering studies of the related compounds $\mathrm{BaMn_2Bi_2}$ [22] and $\mathrm{BaMn_2As_2}$ [23]. The corresponding parameters for these materials are quoted in Table I. The pnictide-coordinated magnetic $\mathrm{Mn^{2+}}$ layers in $\mathrm{BaMn_2Bi_2}$ and $\mathrm{BaMn_2As_2}$ ("122 materials") are analogous to those in the 112 materials investigated in the present paper. However, the $I4/mmm$ 122 compounds do not feature additional pnictide layers (which carry the Dirac bands in the present case). Hence, while the in-plane Mn-Mn spacing is very similar, the spacing of the magnetic layers in the 122 compounds is only 58–66% of that in $\mathrm{CaMnBi_2}$ and $\mathrm{SrMnBi_2}$. Both $\mathrm{BaMn_2Bi_2}$ and $\mathrm{BaMn_2As_2}$ form antiferromagnetically stacked layers of Néel-type order, in analogy to $\mathrm{SrMnBi_2}$. As may be expected from these circumstances, we find that the in-plane exchange interactions in 122 compounds are similar or identical to those in 112 compounds. On the other hand, in the present 112 materials the interplane exchange is significantly reduced. This is consistent with the much higher transition temperatures and the smaller separation of the Mn layers in the 122 materials compared with the 112 compounds.

We find no evidence that the additional Bi layers in 112 materials, which host the Dirac fermions, cause any qualitative changes in the magnon spectrum, such as anomalous broadening or dispersion. The instrument's simulated energy resolution provides an upper bound on the influence of such effects. The characteristics of the Bragg (0.5–1.0 meV) and vanadium (1–4 meV) widths of energy resolution are illustrated in Ref. [14]. By contrast, neutron inelastic measurements of many iron-based superconductors show obvious signatures of a strong hybridization of magnetic and itinerant states. A typical example is $\mathrm{SrFe_2As_2}$ [25], which shows a crossover into the regime of itinerant (Stoner) spin fluctuations. This manifests itself as an increased dampening of spin fluctuations (i.e., a broadening of the neutron spectrum) above a characteristic energy of approximately 80 meV.

As in the 122 compounds, both J_1 and J_2 are positive (antiferromagnetic) in $\mathrm{SrMnBi_2}$ and $\mathrm{CaMnBi_2}$, resulting in frustration between nearest- and next-nearest-neighbor interactions. The theoretical phase diagram of the frustrated J_1-J_2 model on a square lattice has been investigated extensively in the context of iron-based superconductors [26–28]. There is special interest in this phase diagram owing to a possible quantum critical point and spin-liquid phase around $J_2/J_1 \approx \frac{1}{2}$. This regime separates two distinct ordered magnetic phases, with Néel-type order for $J_2/J_1 < \frac{1}{2}$ and stripe antiferromagnetic order for $J_2/J_1 > \frac{1}{2}$. Both 112 and 122 Mn-based compounds exhibit dominant nearest-neighbor exchange, with $J_2/J_1 \approx 0.3$. According to one study the exchange and anisotropy parameters for $A\mathrm{MnBi_2}$ place these materials close to the phase boundary between Néel-ordered and frustrated paramagnetic phases [28]. The resulting quantum fluctuations could explain some of the observed reduction in ordered magnetic moment ($\simeq 3.7\ \mu_{\mathrm{B}}$) compared to the ideal local-moment value of $5\,\mu_{\mathrm{B}}$ [23]. By contrast, in parent compounds of iron-based superconductors such as $\mathrm{BaFe_2As_2}$ and $\mathrm{SrFe_2As_2}$, J_1 and J_2 are of similar magnitude, resulting in stripe-antiferromagnetic order.

V. CONCLUSIONS

In summary, we have performed a comprehensive triple-axis neutron-scattering study of the anisotropic Dirac materials $\mathrm{SrMnBi_2}$ and $\mathrm{CaMnBi_2}$, with the aim of searching for possible influences of the unusual band topology at their Fermi surfaces on their magnetism. In particular, for $\mathrm{CaMnBi_2}$ our previous findings had indicated that the Bi $6p_{x,y}$ bands may play a role in mediating the magnetic exchange between Mn layers.

In both compounds, we observed well-defined magnon spectra consistent with local-moment, semiclassical antiferromagnetism. Using linear spin-wave theory to describe the neutron spectra we have identified and quantified all relevant exchange and anisotropy parameters of a Heisenberg model for the two compounds. In both cases, all details of the dispersion are well reproduced by the model and there is no indication of anomalous broadening or dispersion to within experimental precision. The absolute values of the exchange parameters indicate no substantive differences between the compounds (aside from opposite interlayer coupling).

These results suggest that different routes have to be found to achieve an entanglement of magnetic order and nontrivial band topology. One very promising option is the substitution of magnetic rare-earth ions on the *A* site, providing a more direct interaction with the relevant Bi layers. In particular, a strong response of the transport properties to rare-earth magnetic order has recently been observed in $\mathrm{EuMnBi_2}$ [29], along with the trademark signatures of Dirac transport [30]. Furthermore, recent high-resolution ARPES results and first-principles calculations identify $\mathrm{YbMnBi_2}$ as a type-2 Weyl semimetal with canted antiferromagnetic order [31]. The latter study further suggests that this state would be tuned to a Dirac metal by spin alignment. Naturally, it would be of great interest to perform analogous inelastic neutron studies of the magnetic ground states in those materials.

Note added. After submission of this paper, a Raman spectroscopic study of $\mathrm{SrMnBi_2}$ and $\mathrm{CaMnBi_2}$ was reported by Zhang *et al.* [32]. Raman spectroscopy probes the spin dynamics through a small number of characteristic frequencies which are associated with van-Hove singularities in the two-magnon density of states. The authors of Ref. [32] interpret their data using a similar spin Hamiltonian as in the present paper but without the magnetocrystalline anisotropy term (D in our study). Their analysis yields values for the spin-exchange parameters J_1 and J_2 that are similar to our results, but produces anomalously large values of the interlayer exchange J_c for both materials (one order of magnitude larger than in our paper or in other related materials). The authors of Ref. [32] suggest that this enhanced coupling is caused by the Bi Dirac bands. We would like to draw attention to the fact that the parameters J_1, J_c, and D are strongly correlated in modeling key features of the magnon dispersion [see Eqs. (6) and (7)], so the neglect of D in the Raman analysis could significantly affect the obtained values of J_c. We note that the Raman value of J_c would imply an interlayer dispersion of the one-magnon spectrum at a factor of 11 (Sr) or 7 (Ca) larger than that found here directly by neutron spectroscopy [Fig. 6, Eq. (7)].

ACKNOWLEDGMENTS

We would like to thank Dr. Paul Steffens (Institut Laue-Langevin) for providing the FLATCONE data treatment suite and Dr. Stuart Calder for helpful clarifications on the results reported in Ref. [22]. This work was supported by the U.K. Engineering and Physical Sciences Research Council (Grant No. EP/J017124/1), the Chinese National Key Research and Development Program (Grant No. 2016YFA0300604), and the Strategic Priority Research Program (B) of the Chinese Academy of Sciences (Grant No. XDB07020100). M.C.R. is grateful to the Oxford University Clarendon Fund for provision of a scholarship.

[1] G. Cordier and H. Schäfer, Z. Naturforsch. **32**, 383 (1977).
[2] E. Brechtel, G. Cordier, and H. Schäfer, Z. Naturforsch. **35**, 1 (1980).
[3] J. H. Shim, K. Haule, and G. Kotliar, Phys. Rev. B **79**, 060501 (2009).
[4] J. K. Wang, L. L. Zhao, Q. Yin, G. Kotliar, M. S. Kim, M. C. Aronson, and E. Morosan, Phys. Rev. B **84**, 064428 (2011).
[5] Y. Ran, F. Wang, H. Zhai, A. Vishwanath, and D.-H. Lee, Phys. Rev. B **79**, 014505 (2009).
[6] P. Richard, K. Nakayama, T. Sato, M. Neupane, Y.-M. Xu, J. H. Bowen, G. F. Chen, J. L. Luo, N. L. Wang, X. Dai, Z. Fang, H. Ding, and T. Takahashi, Phys. Rev. Lett. **104**, 137001 (2010).
[7] T. Morinari, E. Kaneshita, and T. Tohyama, Phys. Rev. Lett. **105**, 037203 (2010).
[8] O. Vafek and A. Vishwanath, Annu. Rev. Cond. Mat. Phys. **5**, 83 (2014).
[9] J. Park, G. Lee, F. Wolff-Fabris, Y. Y. Koh, M. J. Eom, Y. K. Kim, M. A. Farhan, Y. J. Jo, C. Kim, J. H. Shim, and J. S. Kim, Phys. Rev. Lett. **107**, 126402 (2011).
[10] Y. Feng, Z. Wang, C. Chen, Y. Shi, Z. Xie, H. Yi, A. Liang, S. He, J. He, Y. Peng, X. Liu, Y. Liu, L. Zhao, G. Liu, X. Dong, J. Zhang, C. Chen, Z. Xu, X. Dai, Z. Fang, and X. J. Zhou, Sci. Rep. **4**, 5385 (2014).
[11] Y. F. Guo, A. J. Princep, X. Zhang, P. Manuel, D. Khalyavin, I. I. Mazin, Y. G. Shi, and A. T. Boothroyd, Phys. Rev. B **90**, 075120 (2014).
[12] K. Wang, D. Graf, L. Wang, H. Lei, S. W. Tozer, and C. Petrovic, Phys. Rev. B **85**, 041101 (2012).
[13] J. B. He, D. M. Wang, and G. F. Chen, Appl. Phys. Lett. **100**, 112405 (2012).
[14] See Supplemental Material at http://link.aps.org/supplemental/10.1103/PhysRevB.95.134405 for the critical exponent analysis, magnetic susceptibility data, analytic expressions for the spin-wave gaps and magnon bandwidths, our procedure used to determine the best-fit spin-wave model, and detailed comparisons between the observed and calculated magnon spectra.
[15] A. Hiess, M. Jiménez-Ruiz, P. Courtois, R. Currat, J. Kulda, and F. Bermejo, Physica B **385–386**, 1077 (2006).
[16] M. Kempa, B. Janousova, J. Saroun, P. Flores, M. Boehm, F. Demmel, and J. Kulda, Physica B **385–386**, 1080 (2006).
[17] Y. Singh, M. A. Green, Q. Huang, A. Kreyssig, R. J. McQueeney, D. C. Johnston, and A. I. Goldman, Phys. Rev. B **80**, 100403 (2009).
[18] M. Tegel, M. Rotter, V. Weiss, F. M. Schappacher, R. Poettgen, and D. Johrendt, J. Phys.: Condens. Matter. **20**, 452201 (2008).
[19] S. D. Wilson, C. R. Rotundu, Z. Yamani, P. N. Valdivia, B. Freelon, E. Bourret-Courchesne, and R. J. Birgeneau, Phys. Rev. B **81**, 014501 (2010).
[20] J. Saroun and J. Kulda, Physica B **234**, 1102 (1997).
[21] J. Saroun and J. Kulda, Neutron News **13**, 15 (2002).
[22] S. Calder, B. Saparov, H. B. Cao, J. L. Niedziela, M. D. Lumsden, A. S. Sefat, and A. D. Christianson, Phys. Rev. B **89**, 064417 (2014).
[23] D. C. Johnston, R. J. McQueeney, B. Lake, A. Honecker, M. E. Zhitomirsky, R. Nath, Y. Furukawa, V. P. Antropov, and Y. Singh, Phys. Rev. B **84**, 094445 (2011).
[24] S. Calder, Quantum Condensed Matter Division, Oak Ridge National Laboratory (private communication).

[25] R. A. Ewings, T. G. Perring, J. Gillett, S. D. Das, S. E. Sebastian, A. E. Taylor, T. Guidi, and A. T. Boothroyd, Phys. Rev. B **83**, 214519 (2011).

[26] M. Mambrini, A. Läuchli, D. Poilblanc, and F. Mila, Phys. Rev. B **74**, 144422 (2006).

[27] J. Richter and J. Schulenburg, Eur. Phys. J. B **73**, 117 (2010).

[28] H.-Y. Wang, Phys. Rev. B **86**, 144411 (2012).

[29] A. F. May, M. A. McGuire, and B. C. Sales, Phys. Rev. B **90**, 075109 (2014).

[30] H. Masuda, H. Sakai, M. Tokunaga, Y. Yamasaki, A. Miyake, J. Shiogai, S. Nakamura, S. Awaji, A. Tsukazaki, H. Nakao, Y. Murakami, T.-H. Arima, Y. Tokura, and S. Ishiwata, Sci. Adv. **2**, e1501117 (2016).

[31] S. Borisenko, D. Evtushinsky, Q. Gibson, A. Yaresko, T. Kim, M. N. Ali, B. Buechner, M. Hoesch, and R. J. Cava, arXiv:1507.04847.

[32] A. Zhang, C. Liu, C. Yi, G. Zhao, T.-l. Xia, J. Ji, Y. Shi, R. Yu, X. Wang, C. Chen, and Q. Zhang, Nat. Commun. **7**, 13833 (2016).